# Mechanical anisotropy of additively manufactured stainless steel 316L: An experimental and numerical study

A. Charmi *, R. Falkenberg, L. Ávila, G. Mohr, K. Sommer, A. Ulbricht, M. Sprengel, R. Saliwan Neumann, B. Skrotzki, A. Evans

*BAM, Bundesanstalt für Materialforschung und -prüfung, Unter den Eichen 87, 12205 Berlin, Germany*

## ARTICLE INFO

## ABSTRACT

The underlying cause of mechanical anisotropy in additively manufactured (AM) parts is not yet fully understood and has been attributed to several different factors like microstructural defects, residual stresses, melt pool boundaries, crystallographic and morphological textures. To better understand the main contributing factor to the mechanical anisotropy of AM stainless steel 316L, bulk specimens were fabricated via laser powder bed fusion (LPBF). Tensile specimens were machined from these AM bulk materials for three different inclinations: 0°, 45°, and 90° relative to the build plate. Dynamic Young's modulus measurements and tensile tests were used to determine the mechanical anisotropy. Some tensile specimens were also subjected to residual stress measurement via neutron diffraction, porosity determination with X-ray micro-computed tomography (μCT), and texture analysis with electron backscatter diffraction (EBSD). These investigations revealed that the specimens exhibited near full density and the detected defects were spherical. Furthermore, the residual stresses in the loading direction were between $-74 \pm 24$ MPa and $137 \pm 20$ MPa, and the EBSD measurements showed a preferential ⟨110⟩ orientation parallel to the build direction. A crystal plasticity model was used to analyze the elastic anisotropy and the anisotropic yield behavior of the AM specimens, and it was able to capture and predict the experimental behavior accurately. Overall, it was shown that the mechanical anisotropy of the tested specimens was mainly influenced by the crystallographic texture.

## 1. Introduction

Additive manufacturing describes layerwise production processes that incrementally build structures from a feedstock material. Laser powder bed fusion (LPBF) is an example of additive manufacturing whereby structures are built in a repeated layerwise fashion via laser-induced localized melting and solidification of a metal powder bed feedstock. These processes offer significantly greater freedom of design compared to conventional subtractive manufacturing processes, with the potential for improved efficiency and functionality [1]. However, despite the technological improvements made in recent years, metal additive manufacturing, also known as metal 3D printing, still faces many different challenges such as microstructural defects, residual stresses (RSs), mechanical anisotropy and in general lack of understanding of process-property-performance relationship [2–4]. These issues are reported to prevent additive manufacturing from mass adoption in safety-critical environments [5].

Stainless steel 316L specimens produced via laser powder bed fusion (LPBF316L) usually have a layered morphology, which consists of many different features on a broad range of length scales [6,7]. Additively

manufactured (AM) alloys and, in particular, LPBF316L have been reported to exhibit anisotropic mechanical properties. The cause of the anisotropic behavior of LPBF316L has been attributed to many different factors. The consequence of layer-by-layer manufacturing, particularly the interface between layers, is one of the more frequently mentioned causes, since oxidation, inclusions, and defects are more frequent in these regions [8–10]. The grain size, grain shape, and grain aspect ratio, in combination with the Hall–Petch effect [11,12], have also been cited as the source of anisotropy in LPBF316L [10,13–15]. The explanation which is usually given for this effect is that the high angle grain boundaries are a major barrier for dislocation glide, and since the dislocations have to cross a different number of grain boundaries in various directions, this results in an anisotropic behavior. However, several authors [6,16,17] consider that the mechanical performance of LPBF316L is mainly determined by its subgrain structures, predominantly the fine-scaled dendritic microstructure, and not by the high angle grain boundaries. Many other research groups reported finding these highly oriented cellular microstructures for different sets of process parameters [6,8,17–22]. RSs [23–27] and melt pool boundaries [28] may also

---

be contributing to the anisotropy of LPBF316L specimens. Crystallographic texture has been repeatedly associated with the mechanical anisotropy of LPBF316L [2,15,29,30]. Moreover, the authors of [13, 17,19,31,32] consider the combination of crystallographic texture and different deformation mechanisms, mainly dislocation slip and twinning, responsible for the directional dependency of material behavior. They argue that for certain specific crystallographic directions defined by the texture, either twinning or dislocation glide are more favorable. Thus, depending on the loading direction, one of the competing mechanisms will dominate the deformation behavior. The authors of [26] investigated the mechanical anisotropy of LPBF316L and compared the results with previous studies. They reported that the observations concerning the orientation dependency of the material behavior differed significantly and even contradictory. For example, in many cases, the highest elongations to failure were obtained in specimens with parallel layers to the loading direction, but in some cases, the specimens with perpendicular layers to the loading direction had the highest elongation after fracture. The dependency of ultimate tensile strength on loading direction also showed no clear tendency [26].

Based on the state of the research, it can be summarized that the underlying cause of anisotropy and the numerical modeling aspect of it in LPBF requires further investigation. Having a better understanding of the origin of anisotropy in LPBF316L is beneficial to the additive manufacturing community when dealing with this issue. Many applications like topology optimization [33,34], modeling of lattice structures [35], and simulation of thermophysical processes during additive manufacturing [36] are heavily influenced by the anisotropy. Hence, the findings in this work could help remedy some of the existing shortcomings and improve modeling accuracy. Therefore, the objective of this paper concerns the determination of the main contributing factor to the mechanical anisotropy of LPBF316L. This investigation was conducted, combining both experimental and numerical methods. Mechanical testing combined with dynamic Young's modulus determination, RS measurements via neutron diffraction, porosity measurements with X-ray micro computed tomography (µCT), and texture analysis with electron backscatter diffraction (EBSD) were used to characterize the material. Numerical simulations were employed to investigate the mechanical anisotropy by only considering the influence of crystallographic texture. Moreover, the comparison between experimental and simulated stress–strain curves will demonstrate the capability of the numerical methods to capture and predict the material behavior accurately.

## 2. Experimental methods

### 2.1. Material and laser powder bed fusion processing conditions

A commercial LPBF system SLM280HL (SLM Solutions Group AG, Germany), equipped with a single 400 W continuous wave ytterbium fiber laser, was utilized to produce specimens using 316L stainless steel powder feedstock. The commercially available gas atomized 316L raw powder can be described by an apparent density of 4.58 g/cm$^3$, and a mean diameter of 34.69 µm according to the supplier information. The cumulative mass values of the particle size distribution were: $D_{10}$ = 18.22 µm, $D_{50}$ = 30.50 µm and $D_{90}$ = 55.87 µm. More details about the powder can be taken from [37,38]. The laser melting processes were conducted in argon gas atmosphere at an oxygen content below 0.1%. The stainless steel base plates were heated up to a temperature of 100 °C before and during the process. The following process parameters were used for all specimens: layer thickness of 50 µm, scanning velocity of 700 mm/s, laser power of 275 W and hatch distance of 0.12 mm. An alternating meander stripe scanning strategy was applied. The scanning pattern was rotated by 90° from layer to layer. Two types of specimens were manufactured in three different build processes: walls of the dimensions $(13 \times 80 \times 80)$ mm$^3$ and towers of the dimensions $(13 \times 20 \times 112)$ mm$^3$, see Figs. 1 and 2. The walls were manufactured upright,

**Table 1**
Overview of all test specimens. Two tensile specimens were manufactured for each loading direction except for the Tower 90°. Young's modulus specimens were manufactured from a single wall.

|  | 0° | 45° | 90° |
|---|---|---|---|
| Tensile specimens from tower | 2 specimens | 2 specimens | 1 specimen |
| Tensile specimens from wall | 2 specimens | 2 specimens | 2 specimens |
| Young's modulus specimens | 1 specimen | 1 specimen | 1 specimen |

the dimension in build direction (Z-Axis) was 82.5 mm in order to compensate for cutting waste during part removal. The towers were manufactured for three different inclinations: 0° (Z-Axis dimension 22.5 mm), 45° (Z-Axis dimension 90.9 mm) and 90° (Z-Axis dimension 114.5 mm) relative to the build plate. The scan vectors proceeded parallel to the edges of the 45° towers and 90° towers over the full length of the part without being split into different sections. For the walls and 0° towers, the scanning vectors proceeded in an angle of 45° to the edges of the respective geometry to avoid high RSs at long scanning vectors and to avoid splitting of scanning vectors into stripes. For a graphical overview of produced geometries, used scan strategies, and coordinate systems, see Fig. 1. The interlayer time (ILT) was kept constant for all processes at a value of approximately 65 s according to [37]. In cases of height differences of specimens that were manufactured on the same base plate or differences in ratios of area exploitations (RAE) between the different build processes, dummy areas were scanned without laser power. All specimens were heat-treated after the process and before removal from the plate at 450 °C for 4 h under argon gas atmosphere to relieve the RSs. This temperature was chosen in order to avoid substantial changes in the microstructure.

### 2.2. Machining of test specimens

To experimentally investigate the mechanical anisotropy, tensile specimens were manufactured from both walls and single towers for three different inclinations, namely 0°, 45° and 90°. Dynamic Young's modulus specimens were only manufactured from the wall. In total, five tensile specimens from five single towers, six tensile specimens from two walls, and three Young's modulus specimens from one wall were produced. An overview of all test specimens can be seen in Table 1. The tensile specimens from the single towers were machined (turned and subsequently ground) from the middle region of each tower. The walls were first symmetrically plane ground to a thickness of 12 mm. Afterward, blocks with near-net dimensions were cut out of the walls via wire electrical discharge machining (EDM). Fig. 3 shows the positions of these blocks, which were subsequently used for producing tensile and Young's modulus specimens. The Young's modulus specimens, which came from the bulk region of the walls (see Fig. 3, on the left), were subjected to milling and surface grinding in the last machining steps. The exact geometry of tensile specimens can be seen in Fig. 3 on the right. The Young's modulus specimens have a dimension of $(3 \times 6 \times 64)$ mm$^3$ with a rectangular cross-section and plane parallelism between the opposite faces with ±1% accuracy. The exact dimensions and weight of the latter specimens, needed for the determination of the elastic properties, were determined with a caliper gauge (Model CD-20D, accuracy: ±10 µm, Mitutoyo Deutschland GmbH, Germany) and an outside micrometer (Model 232871, accuracy: ±1 µm, Vogel Germany GmbH, Germany) and with a precision balance (accuracy: ±0.001 g, Sartorius AG, Germany) respectively.

### 2.3. Tensile testing

The tensile tests were conducted at room temperature according to DIN EN ISO 6892-1 [39] (Method A, strain rate range 2) using a 100 kN Instron testing machine (Model: 4505, Instron GmbH, Germany) calibrated according to DIN EN ISO 7500-1 [40] (Force, class
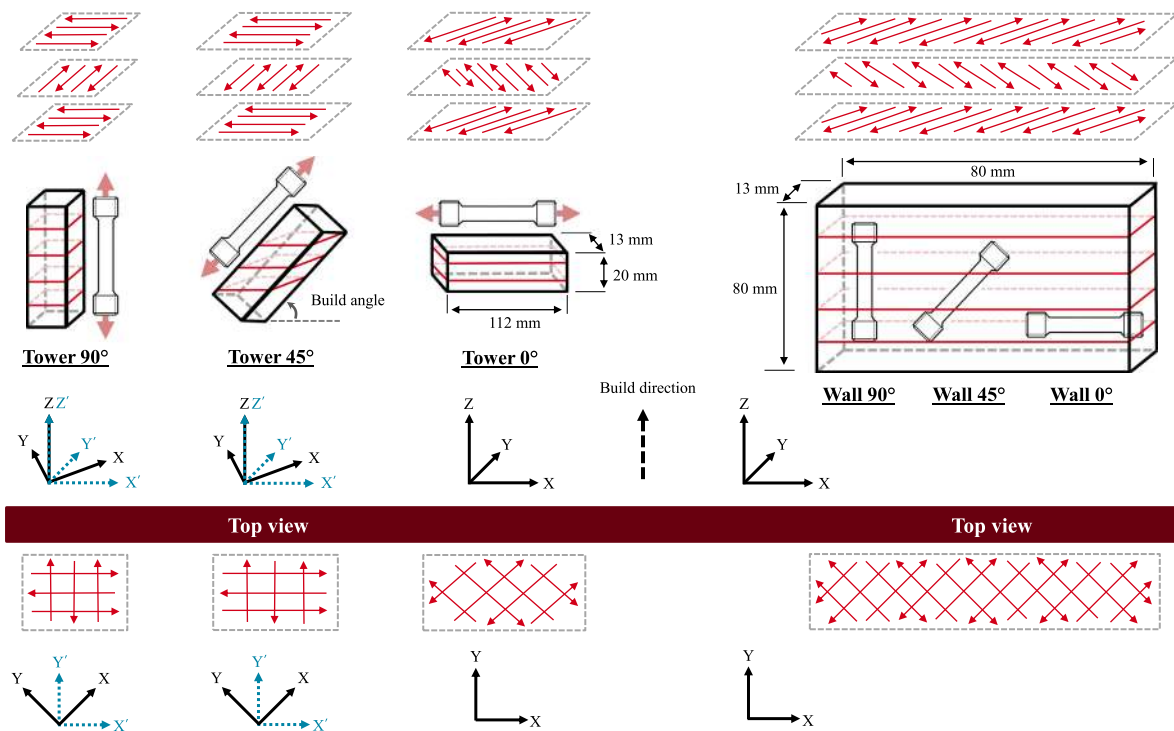
**Fig. 1.** Schematic portrayal of all geometries and the corresponding scan strategies. Note the rotated scan strategy for the Tower 0° and wall specimens compared to the Tower 90° and Tower 45° specimens, which is a 45° rotation about the Z-Axis. These changes were made to avoid high residual stresses and will directly impact the microstructure and consequently, the material behavior, which will be further analyzed in the results and discussion section. The black (X, Y, Z) and blue (X′, Y′, Z′) coordinate systems will be used for the texture analysis in Section 4.3. (For interpretation of the references to color in this figure legend, the reader is referred to the web version of this article.)
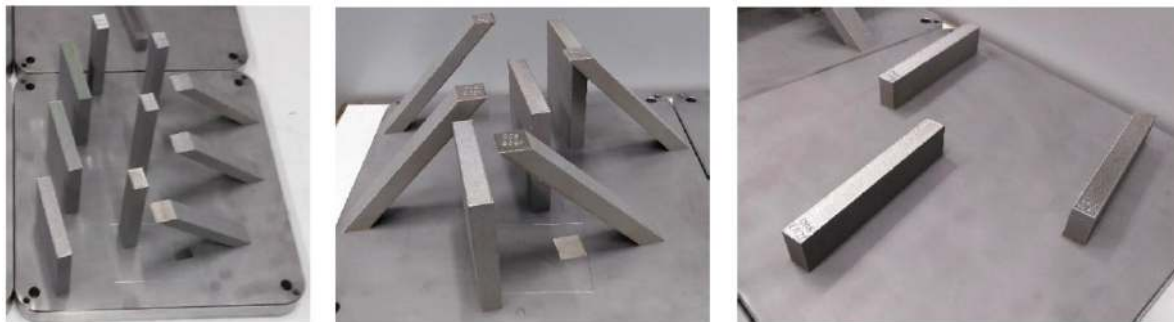


**Fig. 2.** Tower and wall specimens produced during three build processes on $(280 \times 280)$ mm$^2$ base plates. The ILT for each build process was kept at a value of approx. 65 s to ensure comparable thermal history and microstructure across all specimens.

1) and DIN EN ISO 9513 [41] (Displacement, class 1). The strain was recorded using an extensometer (Model: 632.12C-21, MTS Systems GmbH, Germany) with 25 mm gauge length, which was calibrated in the range of −10% to 50% strain according to DIN EN ISO 9513 [41] (class 0.5). Since all specimens failed before reaching the maximum value of the extensometer measurement range, all tests were driven entirely strain-controlled and switching to crosshead speed control was not necessary.

### 2.4. Dynamic Young's modulus determination

The determination of dynamic Young's modulus was carried out at room temperature according to ASTM E1876 [42]. An Industrial testing machine (Model: GrindoSonic MK5, GrindoSonic BVBA, Belgium) and a network analyzer (Model: HP8751A, Agilent Technologies, Inc., United States) were used to perform these tests. In this technique, also called the resonance method, the dynamic Young's modulus is determined using the fundamental resonance frequency, dimensions, and mass of

the test specimens. The dynamic elastic properties are measured under oscillatory displacements, involving small strains, relatively high strain rates, and adiabatic conditions. It should be noted that the elastic properties determined under adiabatic conditions exhibit slightly higher values compared to the elastic properties determined under isothermal conditions [43]. The resonance frequency is measured by exciting the test specimens mechanically by a singular strike with an impulse tool and then analyzing the electric signal generated by a transducer, which senses the resulting mechanical vibrations of the specimen and transforms them into an electrical signal. Dynamic techniques provide an advantage over static methods because of greater precision, ease of specimen preparation, and a wide variety of allowed specimen shapes and sizes [44,45].

### 2.5. Porosity and defects analysis

Microstructural defects are believed by some researchers to play a role in the mechanical anisotropy of AM specimens [8–10]. Therefore,
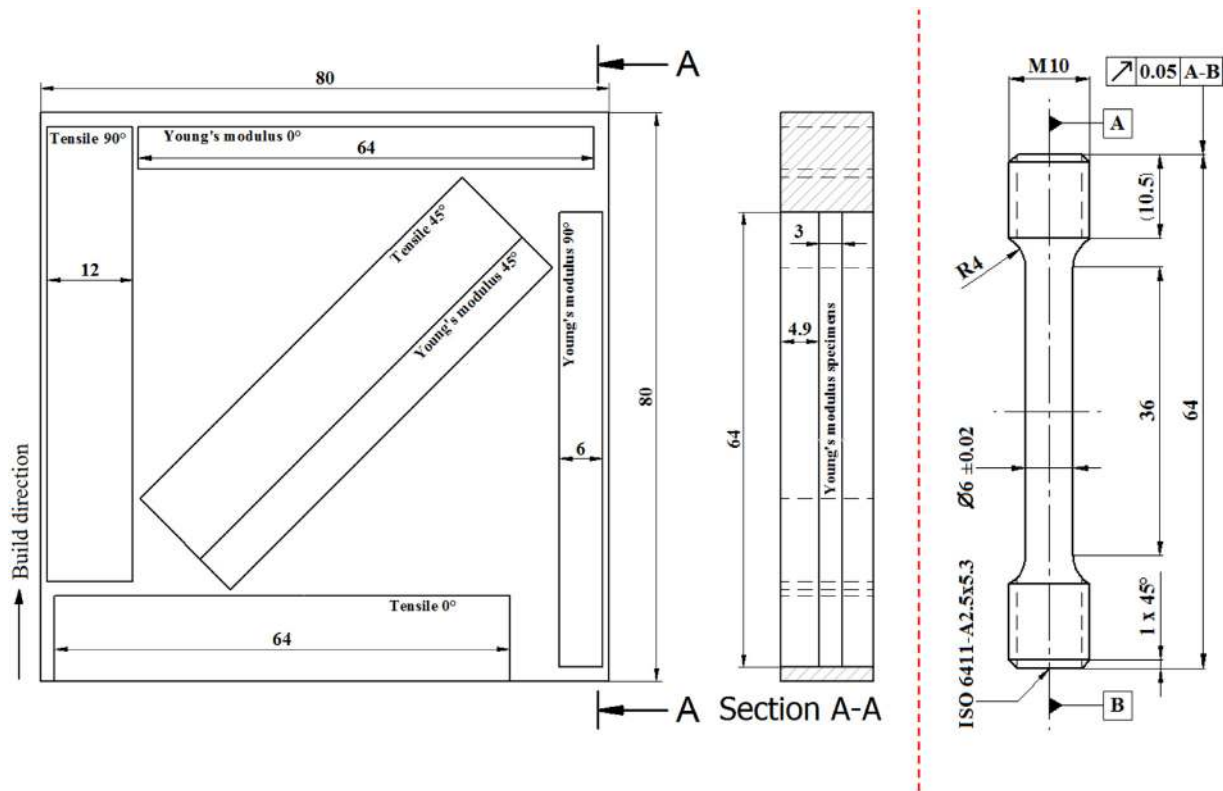
**Fig. 3.** Technical drawings of the test specimens. Position of extracted tensile and Young's modulus specimens in the wall (shown on the left), which were cut out via EDM, and the geometry of tensile specimens (shown on the right).

to assess this possibility within the scope of the process parameters detailed in Section 2.1 and identify the overall quality of the manufacturing process, six of the cylindrical tensile specimens were analyzed for porosity by μCT. Three of them were extracted from towers build with an inclination towards the build plate of 0°, 45°, and 90°, respectively, and three specimens were extracted from a wall with inclinations of 0°, 45° and 90°. The data was acquired on the commercial μCT scanner (Model: GE v|tome|x 180/300, Baker Hughes, United States) using a voltage of 200 kV, a current of 50 μA and a silver prefilter of 0.25 mm thickness. The reconstructed datasets were analyzed using the commercial software VG Studio MAX Version 3.2 (Volume Graphics GmbH, Germany). Pores were segmented within a gauge length of 16 mm around the center of the specimens. Due to the achieved voxel size of 10 μm, only defects larger than 20 μm could be segmented.

### 2.6. Residual stress measurements

The neutron diffraction experiments were performed using the angular-dispersive diffractometer E3 at the Helmholtz Zentrum Berlin, Germany, to determine the state of RSs in six tensile specimens and further investigating their influence on material behavior. The detailed set-up of the instrument can be found in [46]. A wavelength of ≈ 1.476 Å and corresponding $2\theta$ angle of 86° were used to record the Fe-311 reflection. The choice to use the {311} was made based on the reported similar behavior with the bulk properties in the elastic regime as well as its low tendency to form intergranular strains [47–49]. In order to calculate the triaxial RSs, strains were determined along three orthogonal orientations defined by the blank specimen geometry and aligned to the specimen axis. Small cubes of dimension $(3 \times 3 \times 3)$ mm$^3$ were cut by wire EDM close to the gauge length of the specimens extracted from the wall, from the respective specimen blanks or from specimens located in the vicinity of the investigated specimen to be used as the stress-free reference. The use of wire EDM prevents the insertion of additional RSs, as the thin recast layer at the

surface is not sampled, and it is therefore assumed that the macroscopic RSs are fully released in the cubes [48,50]. The stress-free reference diffraction angles were measured in three orthogonal directions and averaged for subsequent stress calculations to minimize the influence of microscopic RSs. The RS distribution for the Tower 90° tensile specimen was acquired during two measurements, and an angular offset of approximately 0.02° related to the different experimental conditions was applied for data merging. The Young's modulus of 184 GPa and Poisson's ratio of 0.294 were calculated in [51] for the {311} reflection assuming random texture using the model of Kröner [52] and measured single-crystal elastic constants. RSs were then calculated using Hook's law:

$$\sigma_{ij} = \frac{E^{hkl}}{1 + \nu^{hkl}} \left( \varepsilon_{ij}^{hkl} + \frac{\nu^{hkl}}{1 - 2\nu^{hkl}} (\varepsilon_{11}^{hkl} + \varepsilon_{22}^{hkl} + \varepsilon_{33}^{hkl}) \right), \qquad (1)$$

with $\sigma_{ij}$ referring to the stress, $E^{hkl}$ and $\nu^{hkl}$ the lattice plane specific Young's modulus and Poisson's ratio, and $\varepsilon_{ij}^{hkl}$ the measured strain. The isotropic condition was used per recently reported work on LPBF316L [51]. However, it is noted that anisotropy of the diffraction elastic constants (DECs) governed by non-random texture would exert an effect on the calculated stresses, although the variation is not considered in the values presented herein. The RSs were determined using a diffraction gauge volume of $(2 \times 2 \times 2)$ mm$^3$ in five measurement positions on three planes distributed along the gauge volume of six tensile specimens. The distance between each plane was 18 mm along the gauge length. The locations of the measurement planes and points in the tensile specimens are shown in Fig. 4. The neutron diffraction data analysis was performed using the StressTexCalculator [53].

### 2.7. Electron backscatter diffraction measurements

For EBSD measurements all specimens were ground and polished: Emery papers with 180, 320, 600 and 1200 grits were used, followed by clothes with 3 μm and 1 μm particle suspensions. Subsequently, the
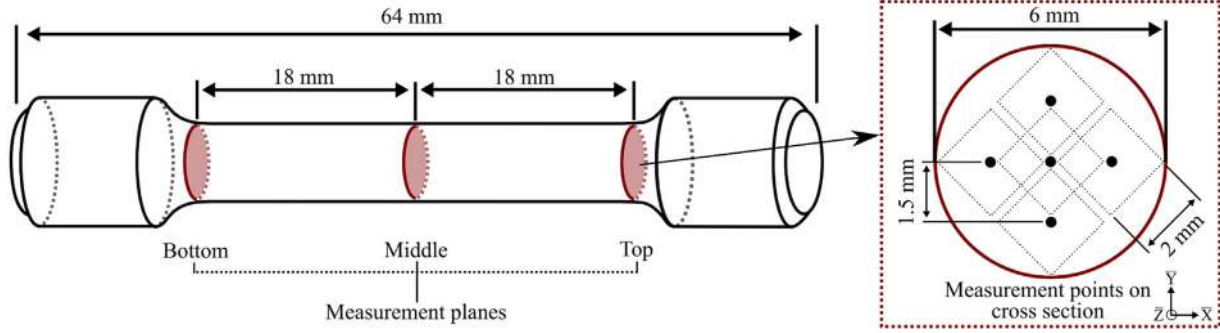
**Fig. 4.** Measurement planes and positions used during neutron diffraction experiments. The RSs were determined on three separate planes along the height of each specimen, which are labeled as Bottom, Middle, and Top. On each plane, five positions were used for the measurements, which are shown on the right side. Note that the sample coordinate system $(\overline{X}, \overline{Y}, \overline{Z})$ is different from the coordinate system in Fig. 1 and it will be used to analyze the residual stresses in Section 4.2. In the sample coordinate system, $\overline{X}$ and $\overline{Y}$ are always parallel to the edges of the produced geometry irrespective of the employed scan strategy. Furthermore, $\overline{Z}$ is always aligned with the loading axis.

specimens were electro-polished on Struers Lectropol-5 (Struers GmbH, Germany) device using standard electrolyte A2. The measurements were done on a scanning electron microscope (SEM) Leo Gemini 1530 VP (Carl Zeiss Microscopy GmbH, Germany) equipped with a high resolution EBSD detector e⁻FlashHR+ (Bruker Corporation, United States). The software package ESPRIT 1.94 (Bruker Corporation, United States) was used for acquisition, indexing and post-processing. The EBSD measurements were done on specimens extracted from the middle section of a Tower 90° specimen, the top section of a Tower 45° specimen, and on specimens extracted from one of the walls. In total five different regions were used for the EBSD measurements to extract the representative crystallographic and morphological texture, see Fig. 5. The 70°-tilted samples were investigated using electrons of 20 kV energy. The further settings for the measurements were 11.9 μm pixel size, 17 ms exposure time, 10 nA beam current, and a pattern size of $160 \times 120$ pixels.

## 3. Numerical methods

### 3.1. Creation of representative volume elements

The simulations in this paper are conducted in a representative volume element (RVE) framework. These RVEs equal the statistical properties of the grain morphology and crystallographic texture, which were extracted from the EBSD scans of the specimens. To simplify this procedure and also isolate the influence of crystallographic texture on the simulation results, the grain size distribution was replaced with a cubic grain having a dimension of $(70 \times 70 \times 70)$ μm³, see Fig. 6. This grain aspect ratio and average grain size are chosen based on the EBSD measurements and the resulting grain size distributions, see Figs. 9 and 11 in Section 4.3. The simulation results for these 3 RVEs were compared to ensure convergence. The synthetic RVEs seen in Fig. 6 were generated with software Neper [54]. The crystallographic texture was extracted from EBSD measurements using the MTEX software [55], which outputs orientation distribution function (ODF) intensity data. The ODFs, which were calculated using a 4.5° halfwidth, were then used in the hybridIA scheme [56] to find discrete sets of orientations matching the number of grains in each RVE. The hybridIA scheme is capable of reconstructing textures using only a few numbers of equally weighted orientations, which is beneficial to the accuracy of crystal plasticity (CP) simulations. In the last step, these extracted orientations were randomly assigned to the Fourier points inside the RVEs.

### 3.2. Mechanical equilibrium

To obtain the equilibrium deformation field, the following equation needs to be solved under a given set of periodic boundary conditions applied to the RVEs:

$$\text{Div } \mathbf{P} = 0, \tag{2}$$

where $\mathbf{P}$ is the first Piola–Kirchhoff stress tensor. The deformation mapping $\chi$ can be decomposed in a homogeneous deformation gradient $\hat{\mathbf{F}}$, and a superimposed deformation fluctuation field $\tilde{\mathbf{w}}$ [57,58]

$$\chi = \hat{\mathbf{F}} \mathbf{x} + \tilde{\mathbf{w}}, \tag{3}$$

which satisfies the periodicity condition. Therefore, the deformation gradient can be split into a homogeneous deformation gradient $\hat{\mathbf{F}}$ and a locally fluctuating part $\tilde{\mathbf{F}}$

$$\mathbf{F} = \hat{\mathbf{F}} + \tilde{\mathbf{F}}. \tag{4}$$

The solution of the mechanical boundary value problem, expressed in terms of the deformation gradient field, is obtained solving the following system of equations [57,58]:

$$\mathscr{F}_{\text{basic}} [\mathbf{F}(\mathbf{x})] := \mathscr{F}^{-1} \left[ \begin{cases} \mathbb{\Gamma}(\mathbf{k}) \, \mathbf{P}(\mathbf{k}) = \mathbf{0} & \text{if } \mathbf{k} \neq 0 \\ \Delta \mathbf{F}_{\text{BC}} & \text{if } \mathbf{k} = 0 \end{cases} \right] \tag{5}$$

where $\mathbf{x}$ and $\mathbf{k}$ are position in real space and frequency vector in Fourier space, respectively. For the sake of brevity, the reader is referred for specifics about the Gamma operator $\mathbb{\Gamma}$ and the collocation-based discretization approach necessary for obtaining Eq. (5) to [57], where the spectral solver of the software DAMASK is described. The boundary conditions for the RVE are prescribed in terms of the deformation gradient $\mathbf{F}_{\text{BC}}$ through the following equation:

$$\Delta \mathbf{F}_{\text{BC}} = \hat{\mathbf{F}} - \mathbf{F}_{\text{BC}}. \tag{6}$$

DAMASK allows also the definition of mixed boundary conditions to avoid non-volume preserving loads for very large deformations. For example a mixed boundary condition for the simulation of tension in 11 direction can be defined through

$$\dot{\mathbf{F}}_{\text{BC}} = \begin{pmatrix} a & 0 & 0 \\ 0 & * & 0 \\ 0 & 0 & * \end{pmatrix} \text{ and } \mathbf{P}_{\text{BC}} = \begin{pmatrix} * & * & * \\ * & 0 & * \\ * & * & 0 \end{pmatrix}, \tag{7}$$

where $a$ is then replaced with a number, which defines the loading rate. The boundary conditions in Eq. (7) can also be used in combination with a rotation matrix to define other loading directions. In this work, $a$ is defined to be $a = 3 \cdot 10^{-4}$, and the different load situations for 0°/45°/90° are realized by the application of rotation matrices.

### 3.3. Crystal plasticity

For the modeling of material anisotropy, the following CP model was applied. The deformation gradient is multiplicatively decomposed in an elastic and plastic part [59]
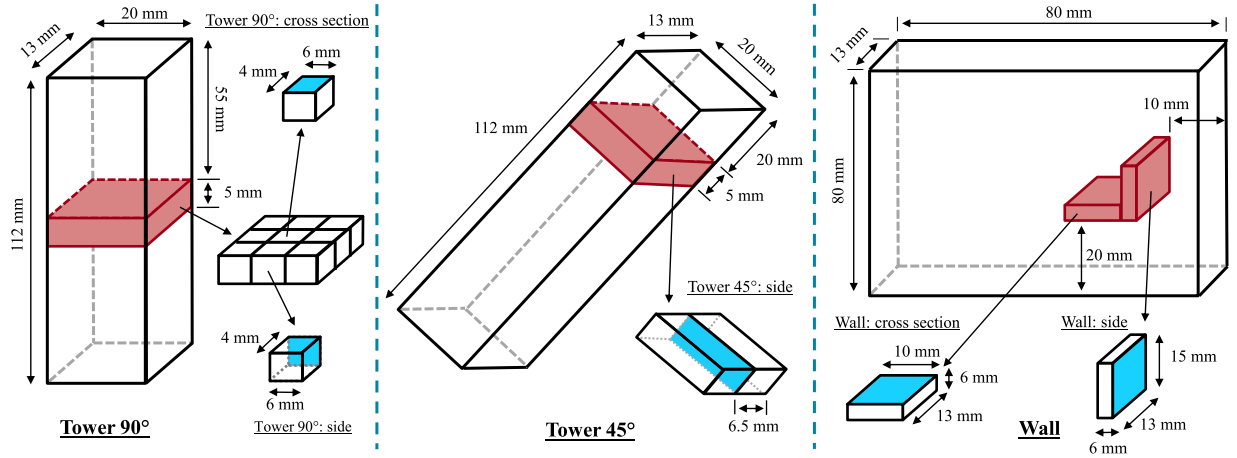
$$\mathbf{F} = \mathbf{F}^{\text{e}} \cdot \mathbf{F}^{\text{p}}. \tag{8}$$

**Fig. 5.** Location of five regions used during EBSD analysis (blue surfaces). Two $(3 \times 4)$ mm$^2$ EBSD measurements were done on specimens extracted from the middle section of a Tower 90° specimen (shown on the left), one $(3 \times 4)$ mm$^2$ EBSD measurement were done on a specimen extracted from the top section of a Tower 45° specimen (shown on the middle) and eight $(3 \times 4)$ mm$^2$ measurements were done on specimens extracted from one of the walls (shown on the right). (For interpretation of the references to color in this figure legend, the reader is referred to the web version of this article.)
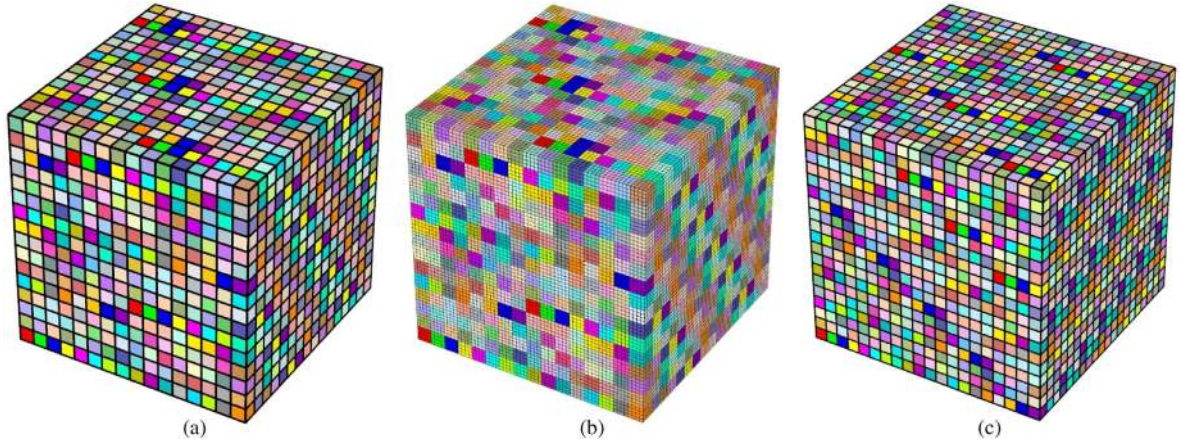


**Fig. 6.** RVEs used for CP simulations. (a) 4096 grains, 1 Fourier point per grain, and dimensions of $(1120 \times 1120 \times 1120)$ μm$^3$, (b) 4096 grains, 64 Fourier points per grain, and dimensions of $(1120 \times 1120 \times 1120)$ μm$^3$, and (c) 8000 grains, 1 Fourier point per grain, and dimensions of $(1400 \times 1400 \times 1400)$ μm$^3$. Note that the colors of the grains do not represent the grain orientation.

The quantities in the intermediate configuration are marked with an overbar ($^-$) and are obtained when the elastic part of deformation is relaxed. Therefore, this state of the body represents a reference configuration for the elastic part of the deformation. The second Piola–Kirchhoff stress $\bar{\mathbf{S}}$ can be written as

$$\bar{\mathbf{S}} = \bar{\mathbb{C}} : \bar{\mathbf{E}}^e, \tag{9}$$

with

$$\bar{\mathbf{E}}^e = \frac{1}{2} \left( (\mathbf{F}^e)^T \cdot \mathbf{F}^e - \mathbf{I} \right) = \frac{1}{2} \left( \bar{\mathbf{C}}^e - \mathbf{I} \right), \tag{10}$$

where $\bar{\mathbb{C}}$ is the fourth order tensor of elastic constants, $\bar{\mathbf{C}}^e$ is the elastic right Cauchy–Green tensor and $\mathbf{I}$ is the identity tensor. The second Piola–Kirchhoff stresses are related to the first Piola–Kirchhoff stresses by $\mathbf{S} = \mathbf{P} \cdot \mathbf{F}^{-T}$. In case of cubic crystals, the elastic tensor $\mathbb{C}$ can be specified with three elastic constants $C_{11}$, $C_{12}$ and $C_{44}$. The total power per unit volume can be decomposed into elastic and plastic parts [60]

$$\dot{w} = \dot{w}^e + \dot{w}^p = \bar{\mathbf{S}} : \dot{\bar{\mathbf{E}}}^e + (\bar{\mathbf{C}}^e \cdot \bar{\mathbf{S}}) : \bar{\mathbf{L}}^p, \tag{11}$$

where $\bar{\mathbf{L}}^p$ is the plastic velocity gradient in the intermediate configuration, which can be written as a function of dislocation glide on different slip systems

$$\bar{\mathbf{L}}^p = \dot{\mathbf{F}}^p \cdot (\mathbf{F}^p)^{-1} = \sum_{\alpha=1}^{N} \dot{\gamma}^\alpha \mathbf{m}_0^\alpha \otimes \mathbf{n}_0^\alpha, \tag{12}$$

where $\mathbf{m}_0^\alpha$ and $\mathbf{n}_0^\alpha$ are unit vectors representing the slip direction and the normal of the slip plane for the slip system $\alpha$, respectively. The plastic power per unit volume can be calculated using the resolved shear stress $\tau^\alpha$ and the slip rate $\dot{\gamma}^\alpha$

$$\dot{w}^p = \sum_{\alpha=1}^{N} \tau^\alpha \dot{\gamma}^\alpha, \tag{13}$$

where $N$ is the number of slip systems. With the Eqs. (11)–(13) the resolved shear stress $\tau^\alpha$ acting on slip system $\alpha$ reads

$$\tau^\alpha = \bar{\mathbf{C}}^e \cdot \bar{\mathbf{S}} : \left( \mathbf{m}_0^\alpha \otimes \mathbf{n}_0^\alpha \right). \tag{14}$$

The employed phenomenological model in this paper utilizes a rate-dependent power-law function to define the slip rate $\dot{\gamma}^\alpha$ [61]

$$\dot{\gamma}^\alpha = \dot{\gamma}_0 \left| \frac{\tau^\alpha}{\tau_c^\alpha} \right|^n \operatorname{sgn}(\tau^\alpha), \tag{15}$$

where $\dot{\gamma}_0$ is the reference shearing rate, $n$ describes the microscopic strain rate sensitivity and $\tau_c^\alpha$ is the slip resistance, which evolves asymptotically from $\tau_0$ towards $\tau_\infty$ [58]. Moreover, to incorporate work-hardening in the material model, the slip resistance $\dot{\tau}_c^\alpha$ is made to be a function of shear rate

$$\dot{\tau}_c^\alpha = \sum_{\beta}^{N} h^{\alpha\beta} \dot{\gamma}^\beta, \tag{16}$$

**Table 2**
Single-crystal elastic constants of stainless steel 316L [62].

| $C_{11}$ (GPa) | $C_{12}$ (GPa) | $C_{44}$ (GPa) |
|---|---|---|
| 206 | 133 | 119 |

**Table 3**
Results from tensile tests according to DIN EN ISO 6892-1 [39].

| | | | 0° | | 45° | | 90° | |
|---|---|---|---|---|---|---|---|---|
| | | | Spec. 1 | Spec. 2 | Spec. 1 | Spec. 2 | Spec. 1 | Spec. 2 |
| $R_{p0.2}$ | MPa | Tower | 583 | 583 | 540 | 537 | 500 | –– |
| | | Wall | 581 | 581 | 564 | 563 | 514 | 506 |
| $R_m$ | | Tower | 692 | 692 | 652 | 653 | 619 | –– |
| | | Wall | 689 | 691 | 670 | 671 | 620 | 611 |
| A | % | Tower | 54 | 55.5 | 56.5 | 56.5 | 60 | –– |
| | | Wall | 56.5 | 56.5 | 56.5 | 53 | 59.5 | 53.5 |
| Z | | Tower | 72.2 | 71.3 | 73.3 | 71.5 | 72.2 | –– |
| | | Wall | 73 | 72.5 | 71 | 70.6 | 72.5 | 72.3 |
| E | GPa | Tower | 212 | 218 | 196 | 199 | 198 | –– |
| | | Wall | 213 | 218 | 194 | 210 | 194 | 181 |

where $h^{\alpha\beta}$ is the instantaneous strain hardening, which can be calculated by a saturation-type law [58]

$$h^{\alpha\beta} = h_0 \left[ q + (1-q)\delta^{\alpha\beta} \right] \left| 1 - \tau_c^\beta / \tau_\infty \right|^a \operatorname{sgn}(1 - \tau_c^\beta / \tau_\infty). \tag{17}$$

The parameters $q$, $h_0$, $\tau_\infty$ and $a$ are the latent-hardening, the reference self-hardening coefficient, saturation value of the slip resistance and the hardening exponent, respectively. The single-crystal elastic constants of stainless steel 316L, which are necessary for the calculation of the elastic tensor $\mathbb{C}$, were taken from [62] and are listed in Table 2.

### 3.4. Parameter identification

The parameter identification was conducted using a least-squares based regression analysis. The residual to be minimized by the Levenberg–Marquardt scheme [63,64] is defined as

$$\text{minimize} \ \ \mathcal{F}(\mathbf{p}) = \frac{1}{2} \sum_{i=1}^{N} w_i (f_i(\mathbf{p}) - y_i)^2 ,$$

$$\text{by changing } \mathbf{p} \in S , \tag{18}$$

$$\text{such that } g_j(\mathbf{p}) \le 0, j = 1, \dots, n_g ,$$

where $\mathcal{F}$ is the residual function, $g_j$ is a vector of constraints, $\mathbf{p}$ is a vector containing the material parameters to be optimized and $w_i$ is the weight associated to experiment $i$. The residual function $\mathcal{F}$ is the least-square distance between experiments and simulations. The vector $\mathbf{p}$ contained the parameters $n$, $h_0$, $a$, $\tau_0$ and $\tau_\infty$. The parameters $q$ and $\dot{\gamma}_0$ were set to a fixed value of 1. During the calibration process only one tensile test (Tower 45°) and one EBSD measurement (Tower 45°) were used, and the strain range was limited with the lower bound of 0 and upper bound of 0.015. The calibrated parameters were validated using the remaining experimental data, see Section 4.5 for more details.

## 4. Results and discussion

### 4.1. Results from tensile tests and resonance method

The characteristic values for each specimen determined in the tensile tests are listed in Table 3 and the corresponding stress–strain curves are shown in Fig. 7.

The results reveal that in general, the characteristic strength parameters (E, $R_{p0.2}$ and $R_m$) increase with decreasing building angle, and there are no significant differences between specimens from walls and towers, except for the 45° orientation, which is considered to be a result of the rotated scan strategy (see Fig. 1) and will be further investigated in following sections. The percentage elongation after

**Table 4**
Results from resonance method according to ASTM E1876 [42].

| | | | 0° | | 45° | | 90° | |
|---|---|---|---|---|---|---|---|---|
| | | | Spec. 1 | Spec. 2 | Spec. 1 | Spec. 2 | Spec. 1 | Spec. 2 |
| E | GPa | Tower | –– | –– | –– | –– | –– | –– |
| | | Wall | 225 | –– | 206 | –– | 180 | –– |

fracture (A) and reduction of area (Z) show no dependency on build orientation. The percentage elongation after fracture (A) is calculated by carefully fitting back together the broken pieces after fracture and measuring the gauge length. It should be highlighted that despite the slight difference between the stress–strain curves for 90° specimens, overall, the tensile tests display a low scatter. By comparing the stress–strain curves, it also becomes clear that each direction has slightly different yield behavior, characterized by the transition from purely elastic to plastic deformation. The 0° direction exhibits the sharpest transition behavior, whereas the 90° specimens display a more diffused transition behavior.

For the resonance method [42] three specimens were cut out from one of the AM walls with three different inclinations towards the build plate. The dynamic Young's moduli were then calculated from the fundamental flexural resonance frequencies obtained from in-plane and out-of-plane flexure and were then averaged. The measurement uncertainty for the dynamic method is around 1%, as previously determined using other materials by inter-laboratory studies. The measured dynamic Young's moduli are listed in Table 4. The results from tensile tests and the resonance method will be analyzed and compared in detail in Section 4.4.

### 4.2. Defects and residual stresses

Six tensile specimens (Tower 0°, Tower 45°, Tower 90°, Wall 0°, Wall 45° and Wall 90°) were investigated via μCT and neutron diffraction to detect the microstructural defects and measure the RSs, since they can have an impact on the material performance of AM parts [27, 65,66]. Table 5 contains the porosity determined for these six tensile specimens. The segmented pores in all the specimens were spherical. Therefore, they are expected to be gas pores. As evident from the very low porosity, it is safe to assume that for the tested specimens in this paper, the microstructural defects do not contribute to the mechanical anisotropy and can, therefore, be omitted in the numerical analysis.

The RSs were also determined in six tensile specimens on three different planes along the height of each specimen. The RSs in normal direction ($\overline{Z}$) of all investigated specimens are shown in Fig. 8. The highest RS range, from maximum to minimum, of all measured specimens was 142 MPa with an average error of approximately 20 MPa. The distribution appears not to be symmetric with respect to the specimen axis. The RS distributions in the specimens 0°, 45° and 90°, all three extracted from one wall, are similar. Minor variations in the RS magnitudes and distributions are considered to be related to the varying extraction locations and orientations within the wall. The specimens extracted from individual towers feature similar RS distributions and magnitudes to the specimens extracted from the wall. The RS magnitudes are lower for Tower 0°, possibly resulting from the increased heat-conducting surface with respect to the low build height or the employed scan strategy, see Section 2.1. The RSs in Tower 90° tend to be compressive, which can be a result of an offset for the stress-free reference, since the RS distribution for this specimen was acquired during two separate measurements. However, the RS range and distribution are not influenced by the reference values and are comparable to the other specimens. The position of the RS profile dictates the occurrence of compressive or tensile RSs, and it strongly depends on the stress-free Ref. [67]. The herein determined RS ranges are low compared to RS ranges of net-shape geometries [50,68,69].
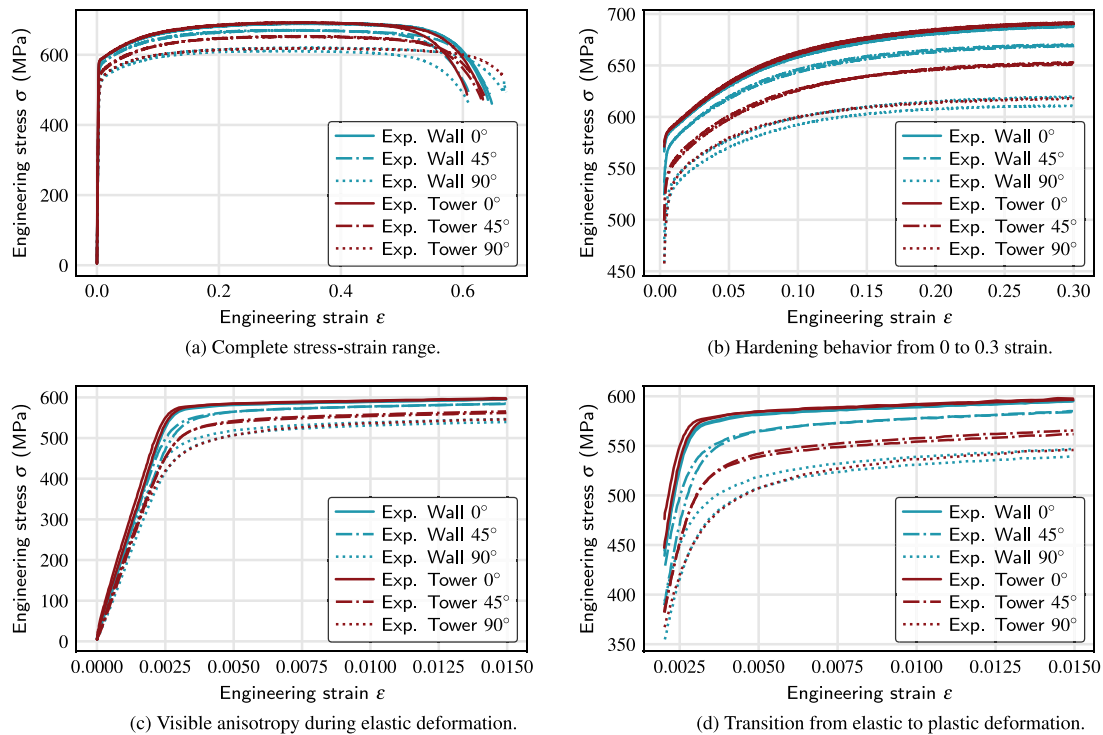
(a) Complete stress-strain range.



(b) Hardening behavior from 0 to 0.3 strain.



(c) Visible anisotropy during elastic deformation.



(d) Transition from elastic to plastic deformation.

**Fig. 7.** Experimentally obtained tensile stress–strain curves. The plots (a, b, c, d) display the same results for different stress and strain ranges, which show that the characteristic strength parameters increase with decreasing building angle. These results also reveal that the stress–strain curves obtained for the Tower 45° and Wall 45° specimens are shifted relative to each other. This difference in the material behavior is due to the rotated scan strategy, see Fig. 1. Additionally, it should be noted that the difference between the stress–strain curves for 90° specimens are not due to a rotation of the scan strategy, since the rotation axis coincides with the loading axis, see Fig. 1. Moreover, the most notable difference is observed for two of the Wall 90° specimens (b). After 0.01 strain, the stress–strain curves for a Tower 90° and a Wall 90° specimen are nearly identical (b, d). Hence, for the analysis in subsequent sections, the specimens are grouped in 0°, Tower 45°, Wall 45° and 90° to account for the effect of the scan strategy.

**Table 5**
Measured porosity by µCT for six tensile specimens. These results indicate that the anisotropy of LPBF316L specimens is not affected by the detected gas pores, since the measured porosity is much smaller than 0.01% for all specimens.

|  | Tower 0° | Tower 45° | Tower 90° | Wall 0° | Wall 45° | Wall 90° |
|---|---|---|---|---|---|---|
| Analyzed volume (mm$^3$) | 443.1586 | 443.7266 | 442.5135 | 443.1867 | 445.1126 | 444.6265 |
| Volume of pores (mm$^3$) | 0.0005 | 0.0015 | 0.0009 | 0.0007 | 0.0013 | 0.0010 |
| Number of pores | 28 | 73 | 42 | 43 | 59 | 57 |
| Porosity | < 0.01% | < 0.01% | < 0.01% | < 0.01% | < 0.01% | < 0.01% |

**Table 6**
Maximum stress range measured in 6 tensile specimens for three orthogonal directions, see Fig. 4 for the used coordinate system. All values are in MPa.

|  | Tower 0° | Tower 45° | Tower 90° | Wall 0° | Wall 45° | Wall 90° |
|---|---|---|---|---|---|---|
| Normal direction ($\bar{Z}$) | 89.98 | 117.64 | 142.68 | 109.5 | 96.81 | 107.49 |
| In-plane direction ($\bar{X}$) | 118.06 | 84.66 | 160.78 | 147.43 | 106.33 | 169.34 |
| In-plane direction ($\bar{Y}$) | 109.3 | 130.75 | 149.92 | 115.31 | 104.87 | 159.31 |

This result can be attributed to mechanical relaxation caused by the machining of the dogbone geometry of the tensile specimens, as reported in [49]. Although possible shifts of the RS distribution profile could occur due to the adopted stress-free reference strategy, the RS ranges determined within this investigation remain low compared to those reported for non-machined structures in LPBF316L [50,68,69], see Table 6. Moreover, it should be highlighted that the tensile specimens were extracted from walls and towers with different geometries and thermal histories, which influence the RSs in each specimen. However, despite the differences in RS profiles, the tensile test results in Fig. 7, in particular for 0° direction, are nearly identical. This behavior is a strong indication that the RSs are not significantly contributing to the mechanical anisotropy of the tested specimens. Therefore, the RSs are omitted during the subsequent numerical analysis.

### 4.3. Texture analysis

In the present study, the texture is determined using EBSD measurements from three different specimens. The measurements were designed to ensure that the derived crystallographic texture is as representative as possible of all the specimens manufactured. Figs. 9–11 contain the EBSD maps, the extracted crystallographic textures, and the grain size distribution for five different regions with a total scanned area of $132\,\text{mm}^2$. The measurements from the wall (both from side and cross-section) each consist of four smaller EBSD maps, which are joined together during post-processing, see Fig. 9(a,b). Note that the EBSD data were subjected to the smoothing algorithm in the software MTEX [55,70] to replace the unindexed measurement points. EBSD maps in Fig. 9 reveal the unusual morphological texture, which is heavily influenced by the employed scan strategy. The morphological texture is recognizable as a checkerboard pattern in the cross-section measurements. Furthermore, the EBSD maps from the side of the specimens display no sign of melt pool boundaries, which is an indication for epitaxial grain growth of remelted zones. Moreover, the comparison between the crystallographic texture extracted from the Tower 90° and the wall, both from side and cross-section, show a three times random {110} texture in the build direction, which is in line with the findings in other studies [13,30,71]. It should be noted that the ODFs extracted from EBSD measurements are dependent on the measurement frame
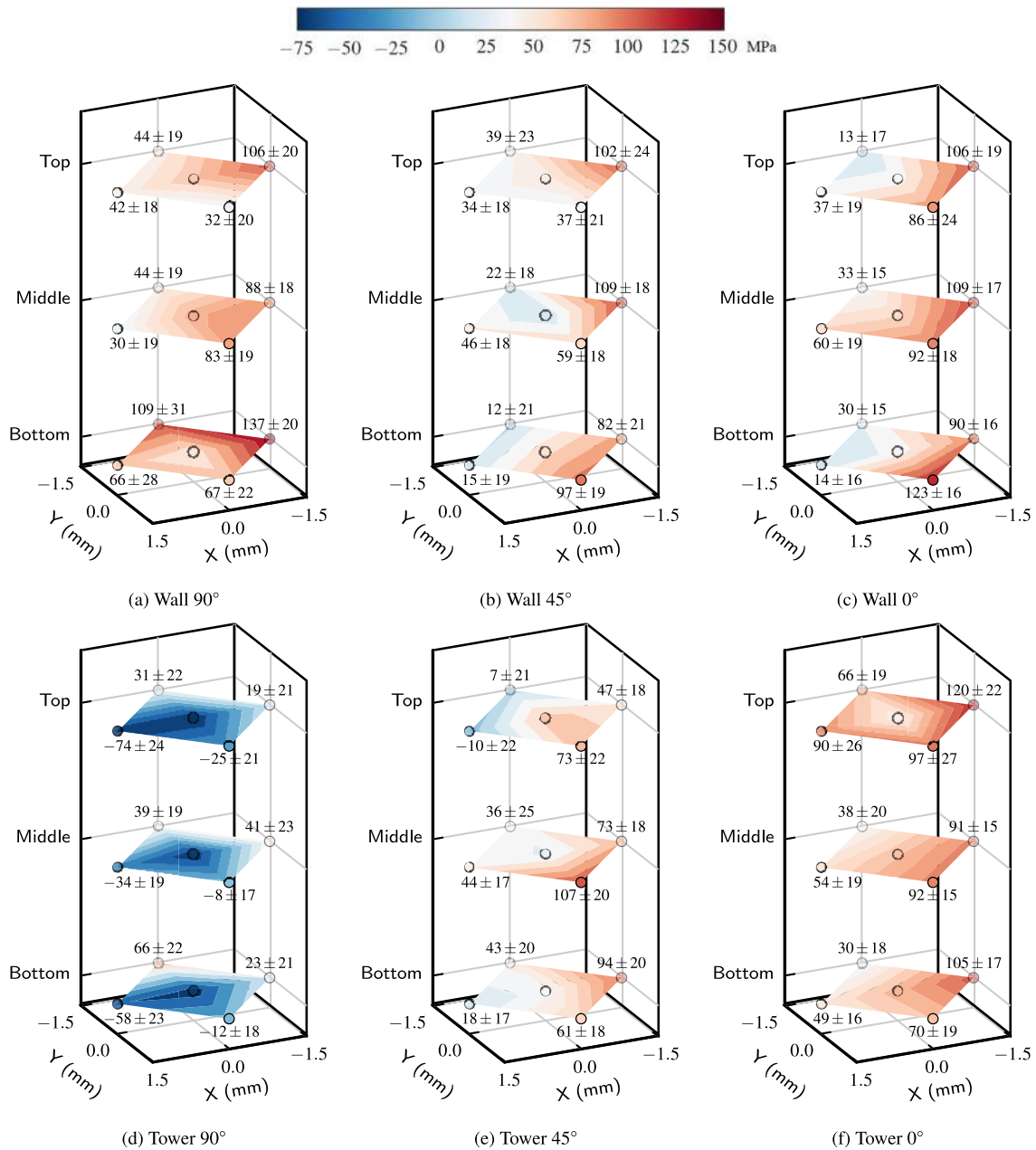
**Fig. 8.** RSs in the normal direction ($\bar{Z}$) measured at different heights. The pictures on the top show RSs in the wall specimens and the pictures on the bottom show RSs in the tower specimens, both for three inclinations. For the used coordinate system, see Fig. 4. The highest value of measured RS is 137 MPa in Wall 90° specimen and the lowest value is −74 MPa in Tower 90° specimen. However, note that the compressive nature of RSs in Tower 90° specimen might be due to an offset for the stress-free reference diffraction values, since the RSs for this specimen were measured during two separate beam times.

and the scan strategy. The ODFs can also be displayed using different coordinate systems. Changing the measurement frame, the scan strategy, or the coordinate system directly impact the outcome. Hence, all the ODFs in the pole figures (Fig. 10) are plotted in the same coordinate system (X, Y, Z) for an easier comparison between the results, see Fig. 1 for all coordinate systems. These five EBSD measurements show that despite the different geometries, crystallographic and morphological textures are very comparable in all manufactured specimens.

### 4.4. Elastic anisotropy

The single-crystal elastic anisotropy of stainless steel 316L can be described through the elastic tensor $\mathbb{C}$ (see Section 3.3), which itself can be specified with three elastic constants $C_{11}$, $C_{12}$ and $C_{44}$. With these values, it is possible to calculate and predict the anisotropic

elastic behavior in any direction. However, this is only applicable to a specimen containing a single grain, since these values are only correct for a single-crystal with a certain crystallographic orientation. The LPBF316L specimens tested in this paper are polycrystalline, as evident from the EBSD measurements, see Fig. 9, and the macroscopic elastic behavior of a polycrystalline specimen is determined by the average behavior of its grains and heavily influenced by the crystallographic texture.

To analyze the macroscopic elastic anisotropy of LPBF316L the Young's moduli were experimentally measured using both tensile testing and resonance method. The Young's moduli, which were determined from eleven tensile tests (see Table 3), were averaged for loading directions 0°, Wall 45°, Tower 45° and 90° and measured to be 215 ± 3 GPa, 202 ± 8 GPa, 198 ± 2 GPa and 192 ± 7 GPa, respectively. The results for Wall 45° and Tower 45° specimens are averaged separately to
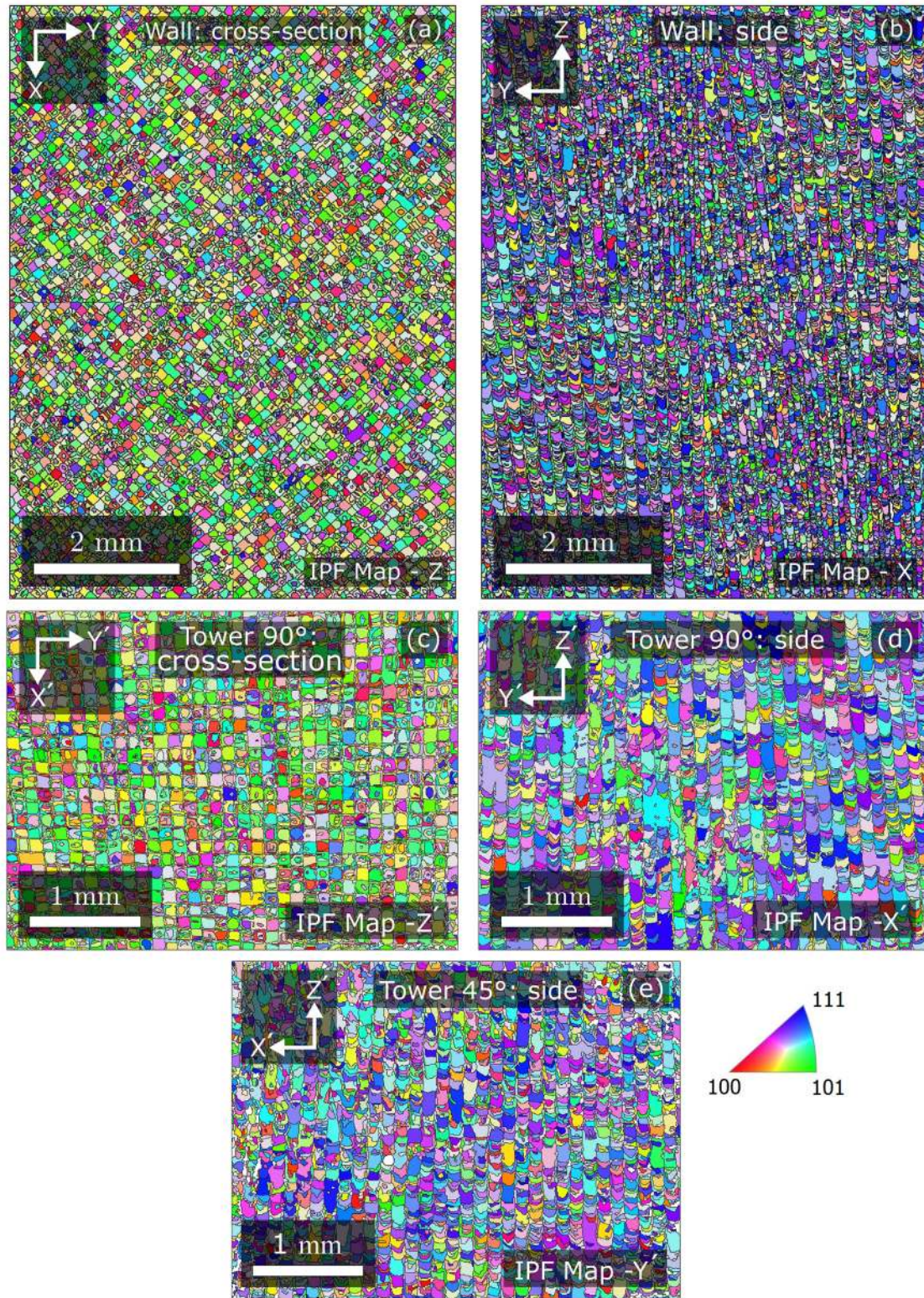
**Fig. 9.** EBSD measurements from cross-section of wall (a), side of wall (b), cross-section of Tower 90° (c), side of Tower 90° (d) and side of Tower 45° (e). Note that the coordinate systems (X, Y, Z) and (X′, Y′, Z′) are different, for more details see Fig. 1. The corresponding pole figures are shown in Fig. 10.

account for the influence of the rotated scan strategy during specimen production, see Figs. 1 and 7. The measured dynamic Young's moduli for Wall 0°, Wall 45° and Wall 90° specimens are 225 GPa, 206 GPa and 180 GPa, respectively.

The macroscopic elastic anisotropy was numerically estimated for all tested directions using the softwares DAMASK [57] and MTEX [55].

The details of the CP model implemented in DAMASK are explained in Section 3.3. The software MTEX has three built-in methods (Voigt, Hill, Reuss) for the estimation of the macroscopic elastic behavior. For the sake of brevity, the reader is referred to [70] for specifics about these methods and the usage of the software MTEX.
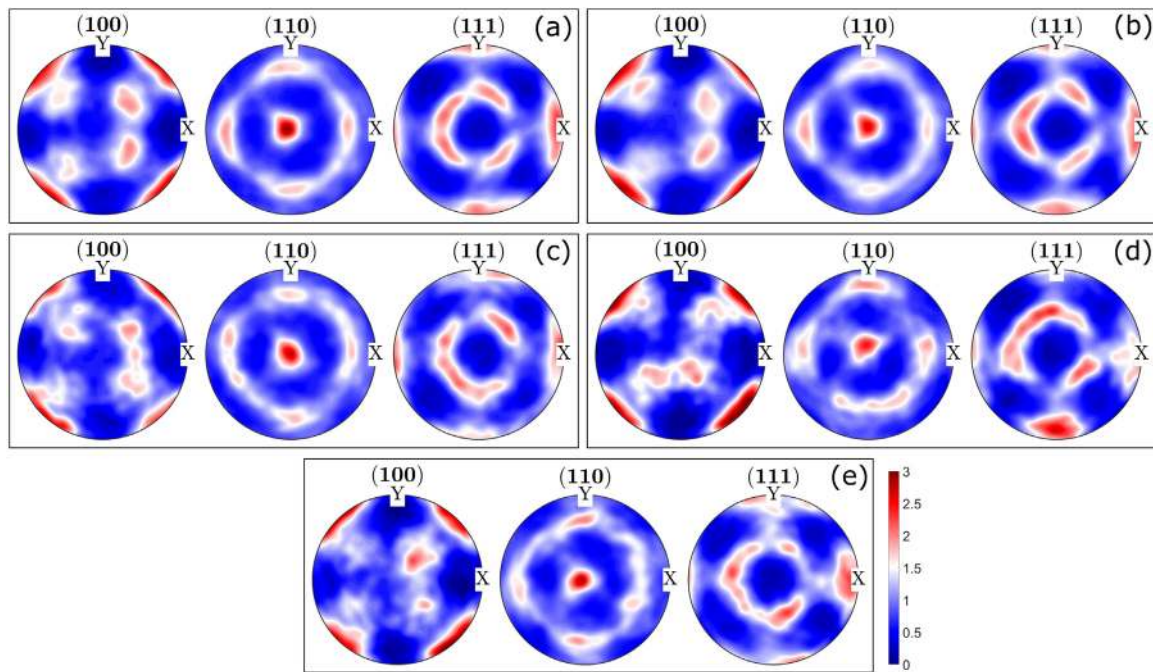
**Fig. 10.** Pole figures from cross-section of wall (a), side of wall (b), cross-section of Tower 90° (c), side of Tower 90° (d) and side of Tower 45° (e). Note that for an easier comparison, all pole figures (a, b, c, d, e) are shown in the same coordinate system (X, Y, Z) and not the coordinate system of their corresponding EBSD map in Fig. 9. It is evident from the results that all specimens have a very similar {110} texture in the build direction.
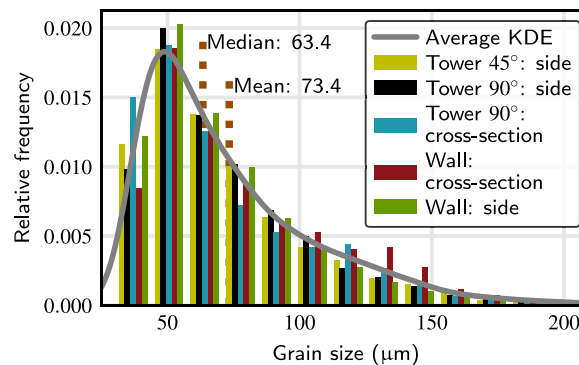


**Fig. 11.** Grain size distributions determined from five EBSD measurements, see Fig. 9. The grain size is calculated from the grain area assuming a rectangular grain shape. The kernel density estimation (KDE) visible in the plot is the average KDE of all five grain size distributions.

For the numerical analysis, the extracted crystallographic textures from all five EBSD measurements and the single-crystal elastic constants of stainless steel 316L from [62] were used, which are listed in Table 2. The experimental and numerical results, which are displayed in Fig. 12, reveal that the Hill estimation approach [70] and the crystal plasticity model are capable of predicting the elastic anisotropy. The numerical results for each estimation method displayed in different colors cover the range between the minimum and maximum value obtained for all five crystallographic textures as slight variations in ODFs influence the numerical results. Furthermore, it should be noted that the observed differences between the results from tensile tests and resonance method might be due to measurement inaccuracies since the employed extensometer for the tensile tests was calibrated in the range of −10% to 50% percent strain and is therefore not perfectly suited for precise measurements of Young's moduli. However, despite these differences, it can be argued that for the tested specimens in this paper, the crystallographic texture is responsible for the elastic anisotropy since the directional dependency of the Young's moduli was captured by only using the crystallographic texture and single-crystal elastic constants as inputs for the simulations softwares. These results are also in line with the findings in [72,73], which showed experimentally and numerically that the elastic anisotropy of their AM inconel 718 specimens were well reflected by the crystallographic texture.

### 4.5. Anisotropic yield behavior

The tensile test results revealed both the elastic anisotropy and also the anisotropic yield behavior of the LPBF316L specimens, see Figs. 7 and 12. In the last section, it was shown that the elastic anisotropy of the tested specimens is highly correlated with the crystallographic texture. The CP model was calibrated using only the tensile test results for the Tower 45° and the EBSD measurement from the side of Tower 45° specimen, see Figs. 7 and 9. The calibration process was done with only a single tensile test and one EBSD measurement to demonstrate the efficiency and reliability of the numerical method. Moreover, the CP model can be calibrated using any of the tensile test results and EBSD measurements. The strain range for the calibration process was between 0 and 0.015. The calibrated parameters of the CP model are listed in Table 7.

The remaining tensile test results and EBSD measurements were used for the validation and sensitivity analysis of the model. The
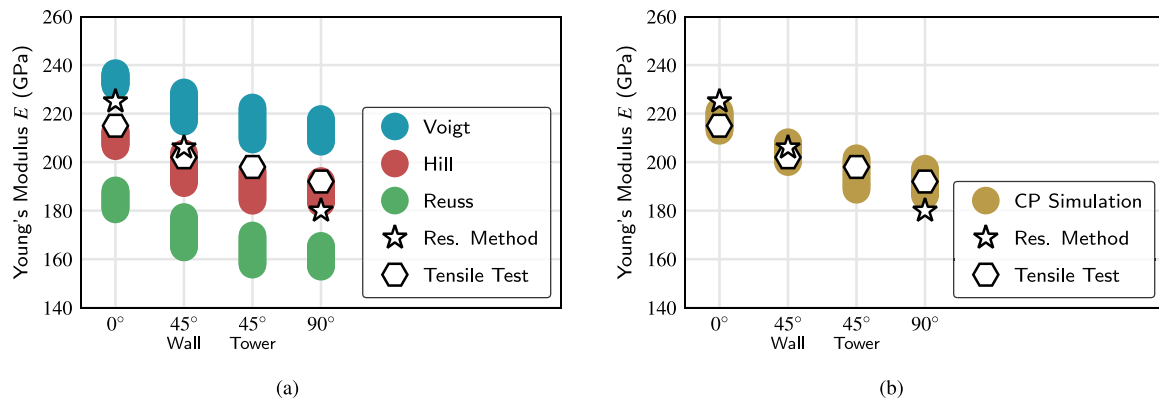
(a)



(b)

**Fig. 12.** Comparison between experimentally measured and numerically estimated Young's moduli using softwares MTEX (a) and DAMASK (b). Each color, which corresponds to a different estimation method, renders the range between the minimum and maximum value obtained for five separate extracted crystallographic textures, see Fig. 10.
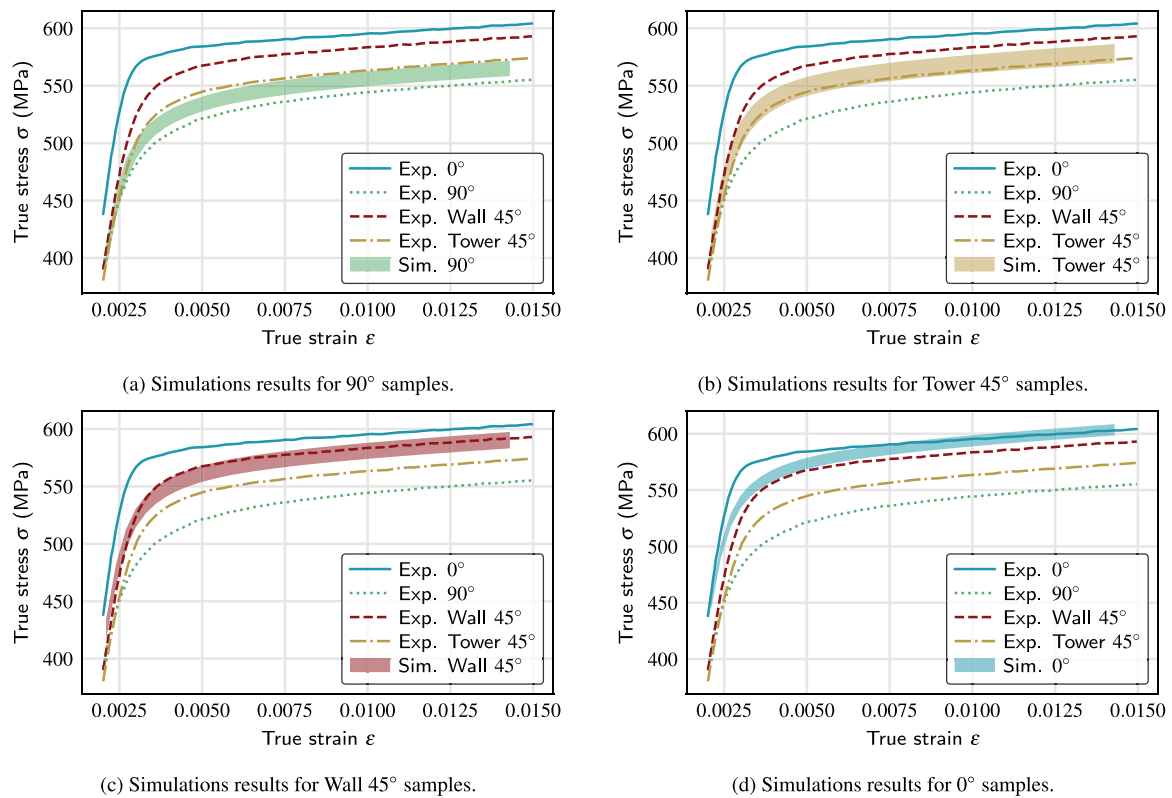


(a) Simulations results for 90° samples.



(b) Simulations results for Tower 45° samples.



(c) Simulations results for Wall 45° samples.



(d) Simulations results for 0° samples.

**Fig. 13.** Comparison between experimental and numerical results (CP) in the strain range of 0.002 to 0.015. The lines represent the experimental stress–strain curves. The plots (a, b, c, d) each contain the simulation results for one specific loading direction. The results for Tower 45° (b) and Wall 45° (c) specimens are displayed separately to account for the influence of the rotated scan strategy during specimen production. The rotation of the scan strategy does not influence the results for the 90° (a) specimens, since the rotation axis coincides with the loading axis, see Figs. 1 and 7 for more details. The simulation results cover the range between minimum and maximum value obtained for all five extracted crystallographic textures, see Fig. 9.

experimental and simulated true stress–strain behaviors for all loading directions and crystallographic textures are plotted in Figs. 13 and 14. The numerical results for each loading direction displayed in different colors cover the range between the minimum and maximum value obtained for all five experimentally determined crystallographic textures, see Fig. 10. As evident in Fig. 7 the tensile test results for each loading direction are very similar. Hence, for easier comparison between the stress–strain curves, only one single tensile test result is plotted for each loading direction. These results show an overall good agreement between the experiments and model prediction.

The maximum deviations between the simulations and experiments are displayed in Fig. 15 as %-error, which demonstrates the accuracy of the numerical model. The %-error is below 5% after only 0.004

strain and stays under 3% after 0.025 strain. These variations are tolerable considering the different sources of measurement error, such as the difficulties of extracting the crystallographic texture from a 2D surface area. Different aspects like surface finish, beam shift, and texture gradients in the material influence the result. Moreover, it should be highlighted that after the model calibration, the same parameter set was used for running all other simulations. This means that the simulation results for textures extracted from the four remaining EBSD measurements can be further optimized since they were not used during the calibration process. However, the main goal of this paper is to demonstrate the sensitivity and reliability of this approach.

Furthermore, it is evident from Fig. 13 that there is a variation in the yield behavior for each loading direction which leads to a greater
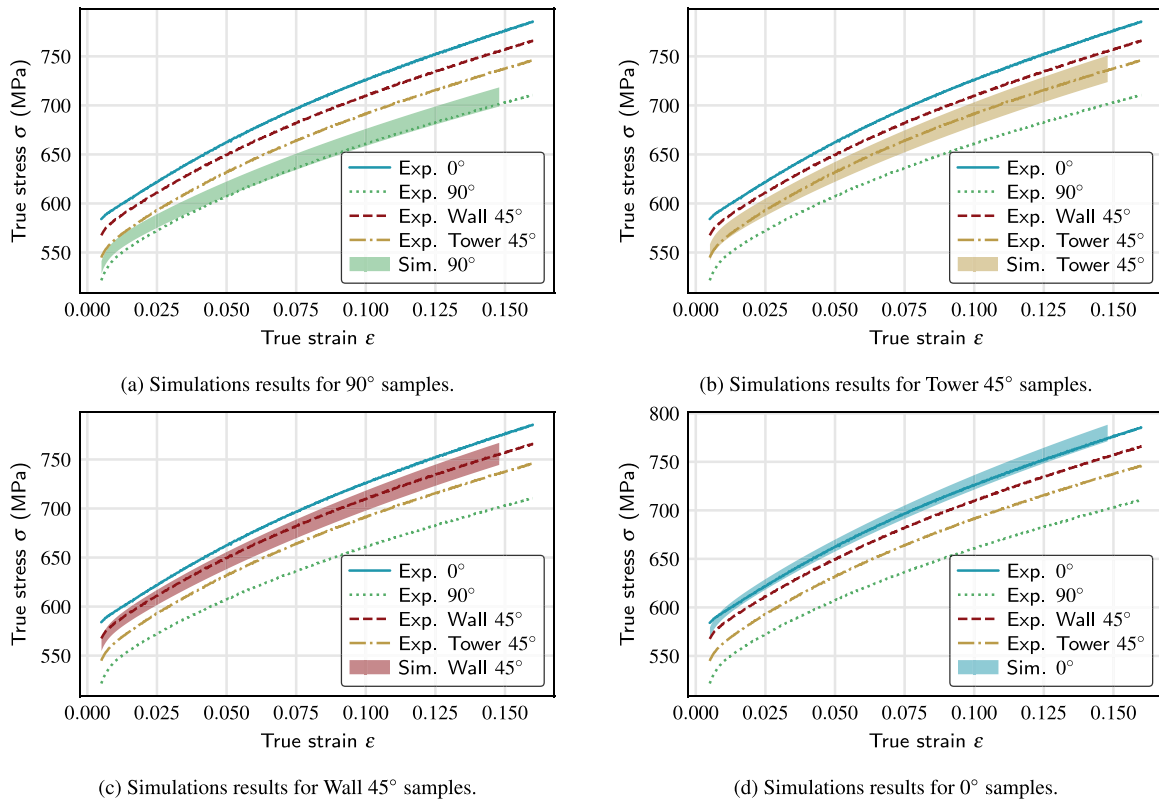
(a) Simulations results for 90° samples.

(b) Simulations results for Tower 45° samples.

(c) Simulations results for Wall 45° samples.

(d) Simulations results for 0° samples.

**Fig. 14.** Experimental and numerical results for all extracted crystallographic textures displayed in the strain range of 0.005 to 0.16, which demonstrate the accuracy of the CP model outside of its calibration range. Note that the strain range for the calibration process was between 0 and 0.015, see Fig. 13.
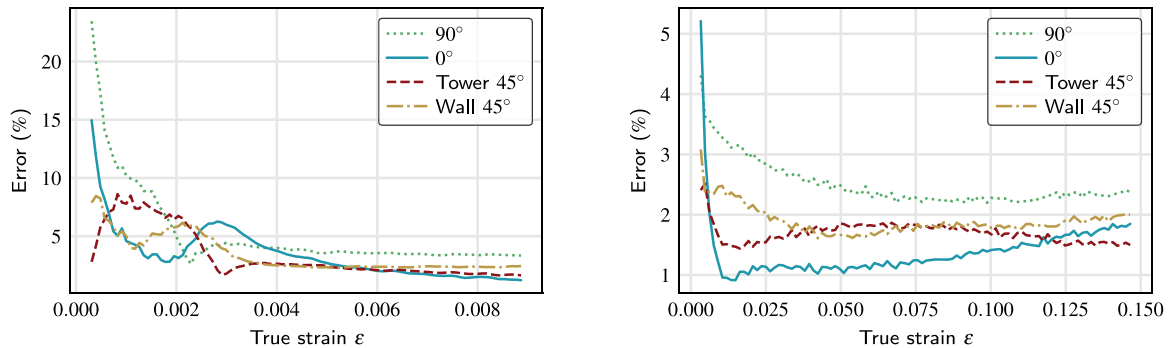


**Fig. 15.** Maximum deviation between the experimental and numerical stress–strain curves (Figs. 13 and 14) presented as %-Error.

deviation between the simulations and experiments, most notably at the beginning of yielding. This behavior might be explained through different competing deformation mechanisms for each particular loading direction. Nano twinning is sometimes the dominating deformation mechanism, as reported in related studies [13,17,19,31]. However, in the currently used CP model only dislocation slip is taken into account. Concluding the findings in this section, the results strongly indicate that the crystallographic texture is the main contributing factor to the anisotropy of LPBF316L, since the CP model was able to accurately capture and predict the anisotropic yield behavior of the tested specimens.

The findings in this section are based on a micro-mechanical crystal plasticity model. Due to the high computational cost, such models can usually only realistically simulate the deformation behavior in small regions, such as the representative volume elements (RVEs) employed in this work. However, additively manufactured parts are orders of magnitude larger than these RVEs. To overcome this constraint, different methods were developed [58,74], which allow these results

to be transferred to the macro-scale. For example, in a virtual-lab framework [58], the calibrated crystal plasticity model can be used to simulate the yield behavior for many different loading conditions. The results of the simulations can in turn be used to calibrate a macroscopic yield surface and thus, allow the use of finite element softwares for simulating the deformation behavior of additively manufactured parts with complex geometries. On a final note, although it is possible to simulate any desired stress state with a calibrated crystal plasticity model, more experimental validation is recommended to ensure the best possible results when simulating complex loading paths. This can be achieved for example using notched specimens or doing shear or torsion tests.

## 5. Conclusions

The mechanical anisotropy of LPBF316L was investigated using both experimental and numerical methods to determine the underlying origin. Several important aspects were examined to isolate the main

**Table 7**
Calibrated material parameters of the CP model.

| $\dot{\gamma}_0 (1/s)$ | $n$ | $h_0$ (MPa) | $a$ | $\tau_0$ (MPa) | $\tau_\infty$ (MPa) |
|---|---|---|---|---|---|
| 1 | 38 | 3160 | 9 | 263 | 1130 |

contributing factor, since the origin of anisotropy in LPBF316L in literature remains inconclusive and exhibits a broad range of explanations.

1. The mechanical testing showed that the yield strength increased with decreasing angle of the building direction relative to the build plate for all tested specimens.
2. EBSD analysis revealed a preferential $\langle 110 \rangle$ orientation parallel to the build direction and a checkerboard morphology, which were a direct result of the layerwise 90° rotation of the scan strategy and were in line with the findings in other studies.
3. The measured porosity in all specimens was much smaller than 0.01%, and the detected defects were spherical. Despite the differences in measured RS profiles, the tensile stress–strain curves for certain loading directions were nearly identical. With these findings, it was concluded that contrary to the statements in some publications, the anisotropy of the tested specimens in this paper is not predominantly controlled by either defects or RSs.
4. Elastic anisotropy was experimentally determined using both tensile testing and resonance method. Through numerical analysis, it was shown that the elastic anisotropy was dominated by crystallographic texture.
5. The anisotropic yield behavior of LPBF316L was modeled using a CP model. The numerical investigations strongly indicated that the directional dependency of yield behavior is mainly governed by the crystallographic texture.

Overall, it can be concluded that the crystallographic texture is the main contributing factor to the mechanical anisotropy of the tested LPBF316L specimens. Moreover, the approach presented in this paper can be employed to accurately capture and predict the mechanical anisotropy of AM specimens in an efficient manner, since it only requires a single tensile test and one EBSD measurement.

## CRediT authorship contribution statement

**A. Charmi:** Conceptualization, Methodology, Formal analysis, Visualization, Validation, Writing - original draft, Writing - review & editing. **R. Falkenberg:** Conceptualization, Supervision, Writing - original draft, Writing - review & editing. **L. Ávila:** Investigation, Resources, Data curation, Writing - original draft, Writing - review & editing. **G. Mohr:** Investigation, Resources, Writing - original draft, Writing - review & editing. **K. Sommer:** Investigation, Formal analysis, Resources, Writing - original draft, Writing - review & editing. **A. Ulbricht:** Investigation, Resources, Formal analysis, Writing - original draft, Writing - review & editing. **M. Sprengel:** Investigation, Resources, Formal analysis, Writing - original draft, Writing - review & editing. **R. Saliwan Neumann:** Investigation, Formal analysis, Resources, Writing - original draft, Writing - review & editing. **B. Skrotzki:** Project administration, Supervision, Funding acquisition, Writing - review & editing. **A. Evans:** Investigation, Project administration, Writing - original draft, Writing - review & editing.

## Declaration of competing interest

The authors declare that they have no known competing financial interests or personal relationships that could have appeared to influence the work reported in this paper.

## Data availability

The raw/processed data required to reproduce these findings cannot be shared at this time as the data also forms part of an ongoing study.

## References

[1] W.E. Frazier, Metal additive manufacturing: A review, J. Mater. Eng. Perform. 23 (6) (2014) 1917–1928.
[2] T. DebRoy, H.L. Wei, J.S. Zuback, T. Mukherjee, J.W. Elmer, J.O. Milewski, A.M. Beese, A. Wilson-Heid, A. De, W. Zhang, Additive manufacturing of metallic components – Process, structure and properties, Prog. Mater. Sci. 92 (2018) 112–224.
[3] P.C. Collins, D.A. Brice, P. Samimi, I. Ghamarian, H.L. Fraser, Microstructural control of additively manufactured metallic materials, Annu. Rev. Mater. Res. 46 (1) (2016) 63–91.
[4] J.J. Lewandowski, M. Seifi, Metal additive manufacturing: A review of mechanical properties, Annu. Rev. Mater. Res. 46 (1) (2016) 151–186.
[5] M. Seifi, A. Salem, J. Beuth, O. Harrysson, J.J. Lewandowski, Overview of materials qualification needs for metal additive manufacturing, JOM 68 (3) (2016) 747–764.
[6] Y.M. Wang, T. Voisin, J.T. McKeown, J. Ye, N.P. Calta, Z. Li, Z. Zeng, Y. Zhang, W. Chen, T.T. Roehling, R.T. Ott, M.K. Santala, P.J. Depond, M.J. Matthews, A.V. Hamza, T. Zhu, Additively manufactured hierarchical stainless steels with high strength and ductility, Nat. Mater. 17 (1) (2018) 63.
[7] E. Liverani, S. Toschi, L. Ceschini, A.A. Fortunato, Effect of selective laser melting (SLM) process parameters on microstructure and mechanical properties of 316L austenitic stainless steel, J. Mater. Process. Technol. 249 (2017) 255–263.
[8] R. Casati, J. Lemke, M. Vedani, Microstructure and fracture behavior of 316L austenitic stainless steel produced by selective laser melting, J. Mater. Sci. Technol. 32 (8) (2016) 738–744.
[9] J. Suryawanshi, K.G. Prashanth, U. Ramamurty, Mechanical behavior of selective laser melted 316L stainless steel, Mater. Sci. Eng. A 696 (2017) 113–121.
[10] D. Kong, X. Ni, C. Dong, L. Zhang, C. Man, X. Cheng, X. Li, Anisotropy in the microstructure and mechanical property for the bulk and porous 316L stainless steel fabricated via selective laser melting, Mater. Lett. 235 (2019) 1–5.
[11] E.O. Hall, The deformation and ageing of mild steel: III discussion of results, Proc. Phys. Soc., London, Sect. A 64 (9) (1951) 747–753.
[12] N.J. Petch, The cleavage strength of polycrystals, J. Iron Steel Inst., London 174 (1953) 25–28.
[13] Y.-D. Im, K.-H. Kim, K.-H. Jung, Y.-K. Lee, K.-H. Song, Anisotropic mechanical behavior of additive manufactured AISI 316L steel, Metall. Mater. Trans. A 50 (4) (2019) 2014–2021.
[14] S. Bahl, S. Mishra, K.U. Yazar, I.R. Kola, K. Chatterjee, S. Suwas, Non-equilibrium microstructure, crystallographic texture and morphological texture synergistically result in unusual mechanical properties of 3D printed 316L stainless steel, Addit. Manuf. 28 (2019) 65–77.
[15] T. Niendorf, S. Leuders, A. Riemer, H.A. Richard, T. Tröster, D. Schwarze, Highly anisotropic steel processed by selective laser melting, Metall. Mater. Trans. B 44 (4) (2013) 794–796.
[16] G.T. Gray, V. Livescu, P.A. Rigg, C.P. Trujillo, C.M. Cady, S.R. Chen, J.S. Carpenter, T.J. Lienert, S.J. Fensin, Structure/property (constitutive and spallation response) of additively manufactured 316L stainless steel, Acta Mater. 138 (2017) 140–149.
[17] C. Qiu, M. Al Kindi, A.S. Aladawi, I. Al Hatmi, A comprehensive study on microstructure and tensile behaviour of a selectively laser melted stainless steel, Sci. Rep. 8 (1) (2018) 7785.
[18] U.S. Bertoli, B.E. MacDonald, J.M. Schoenung, Stability of cellular microstructure in laser powder bed fusion of 316L stainless steel, Mater. Sci. Eng. A 739 (2019) 109–117.
[19] M.S. Pham, B. Dovgyy, P.A. Hooper, Twinning induced plasticity in austenitic stainless steel 316L made by additive manufacturing, Mater. Sci. Eng. A 704 (2017) 102–111.
[20] X. Wang, J.A. Muñiz-Lerma, O. Sánchez-Mata, M. Attarian Shandiz, M. Brochu, Microstructure and mechanical properties of stainless steel 316L vertical struts manufactured by laser powder bed fusion process, Mater. Sci. Eng. A 736 (2018) 27–40.
[21] Michał Zietala, T. Durejko, M. Polański, I. Kunce, T. Płociński, W. Zieliński, M. Łazińska, W. Stepniowski, T. Czujko, K.J. Kurzydłowski, Z. Bojar, The microstructure, mechanical properties and corrosion resistance of 316L stainless steel fabricated using laser engineered net shaping, Mater. Sci. Eng. A 677 (2016) 1–10.

[22] Y. Zhong, L. Liu, S. Wikman, D. Cui, Z. Shen, Intragranular cellular segregation network structure strengthening 316L stainless steel prepared by selective laser melting, J. Nucl. Mater. 470 (2016) 170–178.

[23] Y. Tomota, P. Lukáš, D. Neov, S. Harjo, Y.R. Abe, In situ neutron diffraction during tensile deformation of a ferrite-cementite steel, Acta Mater. 51 (3) (2003) 805–817.

[24] B. Vrancken, V. Cain, R. Knutsen, J. van Humbeeck, Residual stress via the contour method in compact tension specimens produced via selective laser melting, Scr. Mater. 87 (2014) 29–32.

[25] J.V. Gordon, C.V. Haden, H.F. Nied, R.P. Vinci, D.G. Harlow, Fatigue crack growth anisotropy, texture and residual stress in austenitic steel made by wire and arc additive manufacturing, Mater. Sci. Eng. A 724 (2018) 431–438.

[26] L. Hitzler, J. Hirsch, B. Heine, M. Merkel, W. Hall, A. Öchsner, On the anisotropic mechanical properties of selective laser-melted stainless steel, Mater. 10 (10) (2017) 1136.

[27] W. Chen, T. Voisin, Y. Zhang, J.-B. Florien, C.M. Spadaccini, D.L. McDowell, T. Zhu, Y.M. Wang, Microscale residual stresses in additively manufactured stainless steel, Nat. Commun. 10 (1) (2019) 1–12,.

[28] W. Shifeng, L. Shuai, W. Qingsong, C. Yan, Z. Sheng, S. Yusheng, Effect of molten pool boundaries on the mechanical properties of selective laser melting parts, J. Mater. Process. Technol. 214 (11) (2014) 2660–2667.

[29] J.M. Jeon, J.M. Park, J.-H. Yu, J.G. Kim, Y. Seong, S.H. Park, H.S. Kim, Effects of microstructure and internal defects on mechanical anisotropy and asymmetry of selective laser-melted 316L austenitic stainless steel, Mater. Sci. Eng. A 763 (2019) 138152.

[30] Z. Sun, X. Tan, S.B. Tor, C.K. Chua, Simultaneously enhanced strength and ductility for 3D-printed stainless steel 316L by selective laser melting, NPG Asia Mater. 10 (4) (2018) 127–136.

[31] X. Wang, J.A. Muñiz-Lerma, M. Attarian Shandiz, O. Sanchez-Mata, M. Brochu, Crystallographic-orientation-dependent tensile behaviours of stainless steel 316L fabricated by laser powder bed fusion, Mater. Sci. Eng. A 766 (2019) 138395.

[32] Y.J. Yin, J.Q. Sun, J. Guo, X.F. Kan, D.C. Yang, Mechanism of high yield strength and yield ratio of 316 L stainless steel by additive manufacturing, Mater. Sci. Eng. A 744 (2019) 773–777.

[33] L.N.S. Chiu, B. Rolfe, X. Wu, W. Yan, Effect of stiffness anisotropy on topology optimisation of additively manufactured structures, Eng. Struct. 171 (2018) 842–848.

[34] C. Dapogny, R. Estevez, A. Faure, G. Michailidis, Shape and topology optimization considering anisotropic features induced by additive manufacturing processes, Comput. Method Appl. M. 344 (2019) 626–665.

[35] G. Dong, Y. Tang, Y.F. Zhao, A survey of modeling of lattice structures fabricated by additive manufacturing, J. Mech. Des. 139 (10) (2017) 187.

[36] C. Meier, R.W. Penny, Y. Zou, J.S. Gibbs, A.J. Hart, Thermophysical phenomena in metal additive manufacturing by selective laser melting: Fundamentals, modeling, simulation, and experimentation, Ann. Rev. Heat Transf. 20 (1) (2017) 241–316.

[37] G. Mohr, S.J. Altenburg, K. Hilgenberg, Effects of inter layer time and build height on resulting properties of 316L stainless steel processed by laser powder bed fusion, Addit. Manuf. (2020) 101080.

[38] G. Mohr, S.J. Altenburg, A. Ulbricht, P. Heinrich, D. Baum, C. Maierhofer, K. Hilgenberg, In-situ defect detection in laser powder bed fusion by using thermography and optical tomography—Comparison to computed tomography, Metals 10 (1) (2020) 103.

[39] DIN EN ISO 6892-1:2017-02, Metallic Materials - Tensile Testing - Part 1: Method of Test at Room Temperature, Beuth Verlag GmbH, Berlin, Germany, 2017.

[40] DIN EN ISO 7500-1:2018-06, Metallic Materials - Calibration and Verification of Static Uniaxial Testing Machines - Part 1: Tension/compression Testing Machines - Calibration and Verification of the Force-Measuring System, Beuth Verlag GmbH, Berlin, Germany, 2018.

[41] DIN EN ISO 9513:2013-05, Metallic Materials - Calibration of Extensometer Systems Used in Uniaxial Testing, Beuth Verlag GmbH, Berlin, Germany, 2013.

[42] ASTM E1876-15, Standard Test Method for Dynamic Young's Modulus, Shear Modulus, and Poisson's Ratio by Impulse Excitation of Vibration, ASTM International, West Conshohocken, PA, USA, 2015.

[43] H.M. Ledbetter, R.P. Reed, Elastic properties of metals and alloys, I. Iron, nickel, and iron–nickel alloys, J. Phys. Chem. Ref. Data 2 (3) (1973) 531–618.

[44] H.M. Ledbetter, Dynamic vs. static Young's moduli: a case study, Mater. Sci. Eng. A 165 (1) (1993) L9–L10.

[45] M. Radovic, E. Lara-Curzio, L. Riester, Comparison of different experimental techniques for determination of elastic properties of solids, Mater. Sci. Eng. A 368 (1–2) (2004) 56–70.

[46] T. Poeste, R.C. Wimpory, R. Schneider, The new and upgraded neutron instruments for materials science at HMI - Current activities in cooperation with industry, Mater. Sci. Forum 524–525 (2006) 223–228.

[47] M.R. Daymond, M.A.M. Bourke, R.B. von Dreele, B. Clausen, T. Lorentzen, Use of rietveld refinement for elastic macrostrain determination and for evaluation of plastic strain history from diffraction spectra, J. Appl. Phys. 82 (4) (1997) 1554–1562.

[48] F. Bayerlein, F. Bodensteiner, C. Zeller, M. Hofmann, M.F. Zaeh, Transient development of residual stresses in laser beam melting – A neutron diffraction study, Addit. Manuf. 24 (2018) 587–594.

[49] E. Polatidis, J. Čapek, A. Arabi-Hashemi, C. Leinenbach, M. Strobl, High ductility and transformation-induced-plasticity in metastable stainless steel processed by selective laser melting with low power, Scr. Mater. 176 (2020) 53–57.

[50] M. Ghasri-Khouzani, H. Peng, R. Rogge, R. Attardo, P. Ostiguy, J. Neidig, R. Billo, D. Hoelzle, M.R. Shankar, Experimental measurement of residual stress and distortion in additively manufactured stainless steel components with various dimensions, Mater. Sci. Eng. A 707 (2017) 689–700.

[51] P. Rangaswamy, M.L. Griffith, M.B. Prime, T.M. Holden, R.B. Rogge, J.M. Edwards, R.J. Sebring, Residual stresses in LENS® components using neutron diffraction and contour method, Mater. Sci. Eng. A 399 (1–2) (2005) 72–83.

[52] E. Kröner, Berechnung der elastischen Konstanten des Vielkristalls aus den Konstanten des Einkristalls, Z. Phys. 151 (4) (1958) 504–518.

[53] C. Randau, U. Garbe, H.-G. Brokmeier, StressTextureCalculator: A software tool to extract texture, strain and microstructure information from area-detector measurements, J. Appl. Crystallogr. 44 (3) (2011) 641–646.

[54] R. Quey, P.R. Dawson, F. Barbe, Large-scale 3D random polycrystals for the finite element method: generation, meshing and remeshing, Comput. Method. in Appl. Mech. Eng. 200 (17–20) (2011) 1729–1745.

[55] F. Bachmann, R. Hielscher, H. Schaeben, Texture analysis with MTEX – free and open source software toolbox, Solid State Phenom. 160 (2010) 63–68.

[56] P. Eisenlohr, F. Roters, Selecting a set of discrete orientations for accurate texture reconstruction, Comput. Mater. Sci. 42 (4) (2008) 670–678.

[57] F. Roters, M. Diehl, P. Shanthraj, P. Eisenlohr, C. Reuber, S.L. Wong, T. Maiti, A. Ebrahimi, T. Hochrainer, H.-O. Fabritius, S. Nikolov, M. Friák, N. Fujita, N. Grilli, K.G.F. Janssens, N. Jia, P.J.J. Kok, D. Ma, F. Meier, E. Werner, M. Stricker, D. Weygand, D. Raabe, DAMASK – The Düsseldorf Advanced Material Simulation Kit for modeling multi-physics crystal plasticity, thermal, and damage phenomena from the single crystal up to the component scale, Comput. Mater. Sci. 158 (2019) 420–478.

[58] H. Zhang, M. Diehl, F. Roters, D. Raabe, A virtual laboratory using high resolution crystal plasticity simulations to determine the initial yield surface for sheet metal forming operations, Int. J. Plast. 80 (2016) 111–138.

[59] E.H. Lee, Elastic-plastic deformation at finite strains, J. Appl. Mech. 36 (1) (1969) 1–6.

[60] A. Saai, S. Dumoulin, O.S. Hopperstad, O.-G. Lademo, Simulation of yield surfaces for aluminium sheets with rolling and recrystallization textures, Comput. Mater. Sci. 67 (2013) 424–433.

[61] J.W. Hutchinson, Bounds and self-consistent estimates for creep of polycrystalline materials, Proc. R. Soc. A 348 (1652) (1976) 101–127.

[62] H.M. Ledbetter, Predicted single-crystal elastic constants of stainless-steel 316, Br. J. Non-Destr. Test. 23 (6) (1981) 286–287.

[63] K. Levenberg, A method for the solution of certain non-linear problems in least squares, Q. Appl. Math. 2 (2) (1944) 164–168.

[64] J.J. Moré, The levenberg-marquardt algorithm: implementation and theory, in: Numerical Analysis, Springer, 1978, pp. 105–116.

[65] M. Taheri Andani, M. Ghodrati, M.R. Karamooz-Ravari, R. Mirzaeifar, J. Ni, Damage modeling of metallic alloys made by additive manufacturing, Mater. Sci. Eng. A 743 (2019) 656–664.

[66] A. Ahmadi, R. Mirzaeifar, N.S. Moghaddam, A.S. Turabi, H.E. Karaca, M. Elahinia, Effect of manufacturing parameters on mechanical properties of 316L stainless steel parts fabricated by selective laser melting: A computational framework, Mater. Des. 112 (2016) 328–338.

[67] T. Thiede, S. Cabeza, T. Mishurova, N. Nadammal, A. Kromm, J. Bode, C. Haberland, G. Bruno, Residual stress in selective laser melted inconel 718: Influence of the removal from base plate and deposition hatch length, Mater. Perform. Charact. 7 (4) (2018) 20170119.

[68] A.S. Wu, D.W. Brown, M. Kumar, G.F. Gallegos, W.E. King, An experimental investigation into additive manufacturing-induced residual stresses in 316L stainless steel, Metall. Mater. Trans. A 45 (13) (2014) 6260–6270.

[69] P. Mercelis, J.-P. Kruth, Residual stresses in selective laser sintering and selective laser melting, Rapid Prototyping J. 12 (5) (2006) 254–265.

[70] D. Mainprice, R. Hielscher, H. Schaeben, Calculating anisotropic physical properties from texture data using the MTEX open-source package, Geol. Soc. Spec. Publ. 360 (1) (2011) 175–192.

[71] O. Andreau, I. Koutiri, P. Peyre, J.-D. Penot, N. Saintier, E. Pessard, T. De Terris, C. Dupuy, T. Baudin, Texture control of 316L parts by modulation of the melt pool morphology in selective laser melting, J. Mater. Process. Technol. 264 (2019) 21–31.

[72] F. Geiger, K. Kunze, T. Etter, Tailoring the texture of IN738LC processed by selective laser melting (SLM) by specific scanning strategies, Mater. Sci. Eng. A 661 (2016) 240–246.

[73] K. Kunze, T. Etter, J. Grässlin, V. Shklover, Texture, anisotropy in microstructure and mechanical properties of IN738LC alloy processed by selective laser melting (SLM), Mater. Sci. Eng. A 620 (2015) 213–222.

[74] J. Gawad, D. Banabic, A. van Bael, D.S. Comsa, M. Gologanu, P. Eyckens, P. van Houtte, D. Roose, An evolving plane stress yield criterion based on crystal plasticity virtual experiments, Int. J. Plast. 75 (2015) 141–169.